Biosensors and Bioelectronics 77 (2016) 306–314

Contents lists available at ScienceDirect

Biosensors and Bioelectronics

journal homepage: www.elsevier.com/locate/bios

A virus-based nanoplasmonic structure as a surface-enhanced Raman biosensor

Nikolai Lebedev [a,d], Igor Griva [b,d], Walter J. Dressick [a,d], Jamie Phelps [c,d], John E. Johnson [c,d], Yulia Meshcheriakova [a,b,c,d], George P. Lomonossoff [a,b,c,d], Carissa M. Soto [a,d,*]

[a] Center for Bio/Molecular Science and Engineering, US Naval Research Laboratory, 4555 Overlook Avenue SW, Code 6900, Washington DC 20375, USA
[b] Department of Mathematical Sciences and Computational Material Science Center, George Mason University, 4400 University Drive, Fairfax, VA 22030, USA
[c] Department of Molecular Biology,The Scripps Research Institute, 10550, North Torrey Pines Road, La Jolla, California 92037, USA
[d] Department of Biological Chemistry, John Innes Centre, Norwich Research Park, Norwich NR4 7UH, United Kingdom

ARTICLE INFO

Article history:
Received 11 June 2015
Received in revised form
10 September 2015
Accepted 13 September 2015
Available online 21 September 2015

Keywords:
Virus-like particles
Cowpea mosaic virus
Raman
SERS
Gold nanoparticles
Self-assembly

ABSTRACT

Fabrication of nanoscale structures with localized surface plasmons allows for substantial increase in sensitivity of chem/bio sensors. The main challenge for realizing complex nanoplasmonic structures in solution is the high level of precision required at the nanoscale to position metal nanoparticles in 3D. In this study, we report a virus-like particle (VLP) for building a 3D plasmonic nanostructure in solution in which gold nanoparticles are precisely positioned on the VLP by directed self-assembly techniques. These structures allow for concentration of electromagnetic fields in the desired locations between the gold nanoparticles or "hot spots". We measure the efficiency of the optical field spatial concentration for the first time, which results in a *ten-fold* enhancement of the capsid Raman peaks. Our experimental results agree with our 3D finite element simulations. Furthermore, we demonstrate as a proof-of-principle that the plasmonic nanostructures can be utilized in DNA detection down to 0.25 ng/μl (lowest concentration tested), while the protein peaks from the interior of the nanoplasmonic structures, potentially, can serve as an internal tracer for the biosensors.

Published by Elsevier B.V.

1. Introduction

Surface-enhanced Raman spectroscopy (SERS) is a surface-sensitive analytical technique in which the Raman signal intensities of molecules adsorbed onto rough nanostructured noble metal surfaces are significantly enhanced relative to free molecule signals (Schlücker, 2014). Since its discovery in the 1970s, (Fleischmann et al. 1974) the technique has drawn increased attention due, at least in part, to its utility as both a qualitative and quantitative analytical tool, the former by virtue of a species' unique Raman spectrum and the latter by its potential to achieve spectral intensity enhancement factors (EFs) appropriate for single molecule detection. The main challenge in realizing such efficient SERS-active structures is the preparation of composite material architectures exhibiting precisely localized plasmonic interactions. The requisite plasmonic nanostructures are ideally fabricated using noble metal nanoparticles (NPs), which are positioned on or in a supporting inert dielectric structure with controlled nanoscale spacing in well-defined 2D or 3D geometries. Such nanostructures promulgate SERS activity *via* localization and concentration of electromagnetic fields as "hot spots" between adjacent NPs, which facilitate Raman spectral intensity enhancement.

The fabrication of SERS-active architectures has been realized by both "top-down" and "bottom-up" approaches. Top-down approaches often utilize sophisticated techniques such as e-beam lithography, (Aćimović et al. 2009; Bahns et al. 2009) oblique angle deposition, (Driskell et al. 2008; Malvadkar et al. 2010) metallization, (Mu et al. 2010; Shao et al. 2012) and/or etching, (Becker et al. 2009) among others, (Fan et al. 2010; Sarkar et al. 2014; Yang et al. 2015) in combination with wet chemistry to tune plasmon resonance frequencies *via* NP shape (Ortiz and Skrabalak 2014) and composition (e.g., alloy or core–shell species) modifications, (Ferrando et al. 2008; Zhao et al. 2013a) to fabricate 2D SERS architectures on planar surfaces. Such 2D architectures can be fabricated over macroscopic length scales, with SERS EFs $> 10^{13}$ and attomolar analyte detection levels (De Angelis et al. 2011; Tan et al. 2014) achieved for properly designed structures. However, 2D architectures may present limitations for certain applications where the excitation of the plasmons is required to be orientation-independent.

In contrast, 3D architectures are predicted to exhibit orientation-independent plasmonic signatures (Alù and Engheta 2009;

* Corresponding author at: Center for Bio/Molecular Science and Engineering, US Naval Research Laboratory, 4555 Overlook Avenue SW, Code 6900, Washington DC 20375, USA. Fax: +1 202 767 9594.
E-mail address: carissa.soto@nrl.navy.mil (C.M. Soto).

http://dx.doi.org/10.1016/j.bios.2015.09.032
0956-5663/Published by Elsevier B.V.

Barrow et al. 2012; Engheta 2007; Urban et al. 2013) due to their high symmetry. Furthermore, solution-based methods using bottom-up approaches provide a cost-effective alternative for large scale production of 3D plasmonic nanostructures. Bottom-up approaches are dominated by template or scaffolding self-assembly methods more amenable to preparation of freestanding 3D SERS architectures in solution capable of functioning as mobile taggants, tracers, or probes. The simplest such architecture comprises two gold (Au) NPs connected by a molecular linker, (Busson et al. 2011; Wang et al. 2013) though the presence of the linker in the hot spots between the NPs can hinder analyte access. Fortunately, certain high symmetry biomolecules, such as DNA (Barrow et al. 2012; Zhao et al. 2013b) and viral protein capsids (or genetically engineered derivatives thereof), (Zahr and Blum 2012); (Spano et al. 2007) possess sufficiently stable 3D structures bearing surface functional groups capable of binding NPs at precise locations with fixed NP–NP separation distances on their surfaces. NP binding at these sites leads to nanoscale noble metal NP-biomolecule composites in which hindrance of analyte access to the hot spots is minimized. Furthermore, these 3D architectures are ideally sized for interaction with biological materials *in vitro* or *in vivo* and macroscopic surfaces for SERS biosensing.

We have been studying viral protein capsids (Chen et al. 2009; Smith et al. 2013; Soto and Ratna 2010) as scaffolds for fabrication of 3D bio-organic/inorganic nanohybrids for advanced optoelectronics and metamaterials applications (Blum et al. 2004, 2005, 2006, 2007, 2011; Zhou et al. 2012). We recently reported self-assembly of a "BC-nanocluster" (BC-NC) (Fontana et al. 2014) comprising Au NPs (ranging from 17 nm to 34 nm diameter) covalently bound to the surface of 30 nm diameter cowpea mosaic virus (CPMV) protein capsid. The nanostructure exhibits multiple plasmonic interactions among its bound Au NPs consistent with its icosahedral symmetry, with major features of its bulk absorbance spectrum in good agreement with 3D finite-element simulation predictions. Based on our previous findings, in the current work, we utilize 24–30 nm diameter Au NPs to fabricate nanoclusters (NCs) on virus-like-particles (VLPs) and compare them to their BC-NC analogues (Scheme 1). The VLP capsid resembles the wild type (WT) CPMV (Lin et al. 1999) but it lacks the genetic material (RNA) inside the capsid. We selected the VLP as an alternative scaffold based on its similarity to WT-CPMV (available reactive residues on the exterior capsid), its successful utilization in materials applications, (Jaafar et al. 2014); (Aljabali et al. 2010) and lack of nucleic acids that makes it an ideal platform for sensing DNA. We report herein, for the first time, measurements of the SERS response of both of our NCs. Furthermore, when we compare both NCs their SERS responses are similar, paving the way for future use of hollow VLP-NCs as nanoreactors for complex materials preparations and nanostructured 3D assemblies for SERS sensing platforms.

2. Materials and methods

All chemicals were purchased from USA sources and used as received unless otherwise noted. All buffers and aqueous solutions were prepared with deionized water (Milli-Q water; 18 MΩ cm^{-1}). Buffers were filtered sterilized using 0.2 μm Nalgene filters (Fisher Scientific, Pittsburg, PA). *From this point on we will refer to the genetically modified BC-CPMV (60 cys per capsid) as simply BC and the WT-CPMV empty capsid as VLP.* BC was produced by J. Johnson's group and the VLP at G. Lomonosoff's laboratory by methods already published (Sainsbury et al. 2014).

2.1. Hi-trap desalting column, UV-Visible characterization, and quantification

A 5 ml pre-packed Hi-Trap desalting column (GE Healthcare Biosciences, Piscataway, NJ) was equilibrated with 25 ml of appropriate buffer for each application. The column was used for buffer exchange or to remove small molecules from reactions mixtures. Elutions from the column (1.5 ml each; via manual injection of buffer) were evaluated by UV–visible (UV–vis) spectroscopy to identify the capsid-containing fraction. A Cary 5000 UV–vis–NIR spectrometer (Agilent Technologies, Santa Clara, CA) was used for all UV–vis spectroscopy measurements using 1 ml disposable cuvettes (Fisher Scientific). Quantification of the capsids was based on the absorbance peak of the capsids (λ max) and corresponding extinction coefficient (ε). For the VLP: λ max is 280 nm, ε=1.28 ml mg^{-1} cm^{-1} and for BC: λ max is 260 nm, ε=8 ml mg^{-1} cm^{-1}.

2.2. Dynamic light scattering (DLS)

Particle size was determined using a Brookhaven Instruments ZetaPALS dynamic light scattering (DLS) system equipped with a 658 nm diode laser, using 1 cm path-length cuvettes. Three milliliters of sample were used. Ten measurements were taken per data

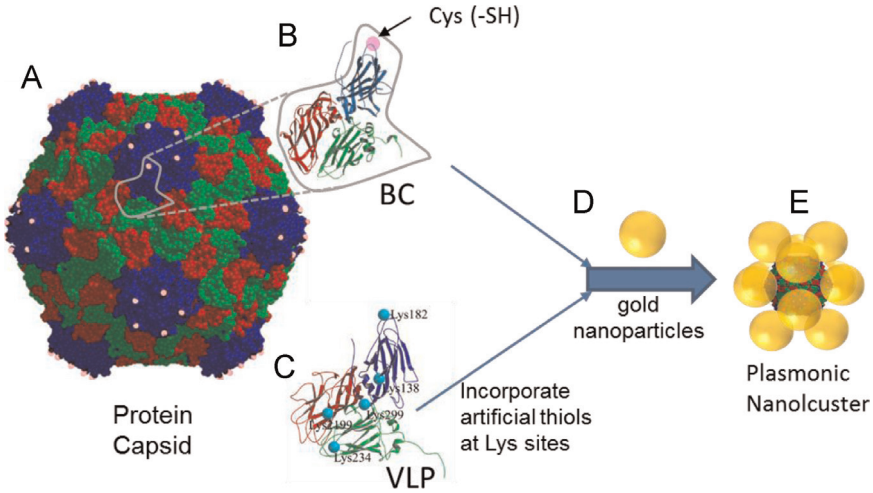

Scheme 1. Plasmonic Nanoclusters synthesis. (A) The protein capsid (30 nm in diameter) generated from the PDB file (1NY7). (B) Protein subunit where pink circles represent Cys incorporated *via* genetic engineering for a total of 60 thiols per capsid, BC-mutant. (C) Protein subunit of the VLP showing the locations of the natural-occurring Lys, artificial thiols are incorporated at the Lys sites using known chemistries. (D) Gold nanoparticles (24–30 nm in diameter) are bound to the VLP or BC by directed self-assembly resulting in (E) plasmonic nanoclusters. Structures are not drawn to scale.

point at 25 °C.

2.3. Nanoclusters (NC) fabrication

Protected-artificial thiols (SHR) were incorporated into the VLP by similar methods previously reported (Soto 2014; Steinmetz et al. 2007) for the WT-CPMV using the linker N-Succinimidyl S-acetylthiopropionate (SATP; Thermo Scientific Pierce, Rockford, IL). Deprotection was performed using hydroxylamine just prior to Au NP coupling. For easy accessibility to all the experimental details about fabrication, purification, and characterization see the Supplementary Information.

2.4. Surface modification: Silane–mica surface

N-[3-(trimethoxysilyl)propyl]ethylenediamine (EDA) from Sigma-Aldrich was vacuum distilled (140 °C; 15 mm Hg) immediately prior to use. Glacial acetic acid was TraceSELECT™ Ultra grade (> 99.99%) used as received from Sigma-Aldrich. Chemisorption of the EDA self-assembled monolayer (SAM) onto the mica substrates was accomplished using the literature procedure (Dressick et al. 1996) with slight modification, as described below. Briefly, an EDA solution was prepared immediately prior to use by addition of 1 ml of freshly distilled EDA to 99 ml deionized water, followed by addition of 200 µl glacial acetic acid as a catalyst with stirring. A 100 µl aliquot of the EDA solution was dispensed onto the freshly cleaved surface of a mica substrate (1 cm diameter disks, Muscovite Mica, V-1 quality, Electron Microscopy Science, PA) residing in a Petri dish inside a constant humidity chamber (100% R.H.). The EDA solution was allowed to stand on the fresh surface of the mica inside the closed chamber for 30 min. After this time, the EDA solution was carefully removed from the mica (a plastic pipet was used during all the washes steps to avoid damaging the mica) and discarded. The sample was immediately washed by dispensing a 100 µl aliquot of water onto the mica surface. After 1 min, the wash water was carefully removed from the mica surface and discarded. The treated mica surface was washed three times in this manner. After the final water wash, the mica substrate was carefully blown dry using a N_2 gas stream (liquid N_2 boil-off) and placed in an oven for 6 min at 110 °C to complete the drying and EDA chemisorption process. The EDA-coated mica substrate was allowed to cool to room temperature, labeled on its untreated side, and stored in a tightly sealed Fluoroware™ container until needed for experiments. For treating 1×1 in^2 mica surface (Muscovite Mica, V-1 quality, Electron Microscopy Science, PA) the same protocol was used with the exception that both sides of the mica were cleaved and treated simultaneously by submerging the 1×1 in^2 surface in a Coplin jar containing the corresponding solutions for treatment or washes.

2.5. Samples preparation for AFM and SERS analysis

BC-NC and VLP-NC recovered from agarose gels (Supplementary Information) were washed 2 × with 10 mM Bis-Tris, 1 mM EDTA, pH 6.5 buffer using 100 k centrifugation filters and diluted back to its original volume with the same buffer (for a typical reaction the final volume is 2 ml). One microliter of BC-NC or VLP-NC in buffer was placed on a silane–mica substrate and let dry at room temperature (~20 min) then washed 3 × gently by submerging the surface in Milli-Q water for 5 s. The surfaces were dried at RT prior to AFM or SERS experiments.

A 4×4 array (on a 1×1 in^2 silane–mica substrate) was prepared (Supplementary Scheme S1) for SERS DNA detection experiments. One microliter of BC-NC (OD ~ 0.2 at 535 nm) was placed on the silane-mica substrate, let dry and washed 3 × with water. A paper map of the array (Supplementary Scheme S1) was kept under the transparent mica to be able to place the DNA on top of the area were the BC-NC was dried. M13mp18 circular ssDNA solutions (7249 nucleotide bases, 1 µg of M13mp18 = 0.21 pmol = 1.3×10^{11} molecules from New England Biolabs, MA) were prepared by diluting the 250 ng/µl commercial ssDNA solution in water (RNAse-free) down to 25, 2.5, and 0.25 ng µl^{-1}. We were able to detect DNA in all the areas where the DNA was placed on top of the BC-NC. As a negative control for DNA detection, 1 µl of the 250 ng µl^{-1} DNA was dried on silane-mica.

2.6. Atomic force microscopy (AFM) imaging

Samples for AFM analyses were prepared on silane–mica surfaces and were the same as for Raman analyses. The AFM experiments were performed with JSPM-5200 microscope (JEOL-USA, Peabody, MA) in alternative current amplitude and phase modes allowing for avoiding sample alteration by AFM tips and increasing image spatial resolution. The experiments were performed in air at 22 °C with dried samples with silicon Tap-300 AFM probes (BudgetSensors, Sofia, Bulgaria) having force constant 40 N/m. The AFM was operated at oscillation frequencies approximately 320 KHz (Q-factor of approximately 562) at a scan speed approximately 3 µm/s with feedback filter 1.20–1.60 Hz. ***Control measurements performed at high resolution AFM show no sample damage before and after experiments***. Image processing was done with JEOL SPM software. The same software was used to determine surface coverage and particle height distributions.

2.7. Calculation of electromagnetic field density

To calculate distribution of the electromagnetic (EM) field around NCs we used Maxwell's equations solved with a finite element method in 3D space (Jin 2002). Twelve Au NPs of 30 nm diameter were placed uniformly around a central sphere of diameter 30 nm. The resulting gold cluster was placed in the cubic vacuum domain of the size length of 150 nm with the absorbing boundary conditions at each of 6 sides (Jin 2002). The mesh was designed consisting of 488 elements for each of 12 spheres and 15910 elements for the rest of the domain. We used frequency dependent empirical dielectric constant for gold taken from the literature (Palik 1998). The calculations were performed for 785 nm excitation light. The result of the calculation was the space dependent electric field amplification $|E|/|E_{incedent}|$ with electric vector of incident light intensity 1 W/m. A Dell Workstation Precision 7200 64 bit with Dual Quad Core Intel Xeon processors having 48 Gb RAM was used for this calculation.

2.8. Spatially resolved confocal Raman spectroscopic (SERS) analysis

Preliminary 4×4 arrays (Supplementary Scheme S1) were prepared to determine the optimum concentration and volume applied on the surface for optimum visualization of the NCs. The criteria to analyze the NCs individually was to have NCs far from each other (~1 µm) on the surface as visualized by the bright light generated from the scattering of the Au NPs on the NCs. The optimum conditions were found to be 1 µl of a NC solution of ~0.2 OD at 535 nm. Raman spectra were collected with a Renishaw in via Raman microscope (Hoffman Estates, IL) with 100 × objective and laser light 785 nm (with pinhole) (Lebedev et al. 2014b). The excitation energy was kept below 0.06 mW. Each spectrum was recorded three (3) times and averaged, and standard deviations for virus proteins intensity profiles were calculated from normalized virus protein peaks to the mica substrate. Though only 3 single scans were performed at each sample point, in some cases up to 10 similar spectra were averaged to improve the spectral resolution

and check spectral variability. The spectral data processing (smoothing, averaging, and background subtraction, if needed) were performed with IgorPRO data analysis software (WaveMetrics, Portland, OR).

3. Results and discussion

In our previous work, (Fontana et al. 2014) we genetically engineered a BC mutant bearing five cysteine (Cys) residues pentagonally oriented on each icosahedral face of the CPMV capsid (a total of 60 Cys per capsid), facilitating covalent binding of Au NPs at the Cys thiol sites to self-assemble the BC-NC (Schemes 1A and B). In the current work, for the VLP capsids, we chose a chemical approach amenable for manufacture (Scheme 1C). Specifically, a reaction of naturally occurring lysine (Lys) residues on the surface of the icosahedral capsid (Chatterji et al. 2004) with SATP followed by hydroxylamine hydrolysis provides thiol groups for Au NP binding (Schemes 1D and E, Supplementary Fig. S1 and S2). The resulting VLP-NCs exhibit a visible absorbance spectrum similar to the BC-NCs (Fig. 1A). In particular, both NCs, in *bulk* solution, exhibit plasmon absorption peaks red-shifted in comparison to free Au NPs (Fig.1A), together with a broad band in the 600–675 nm region amenable for specific longitudinal surface plasmon (LSP) excitation for SERS studies.

DLS measurements (Figs. 1B and C) further indicate that, as expected, both NCs are substantially larger than the Au NPs. It is important to note that the size of the VLP-NC, reported for the first time herein (major scattering peak centered at 78 nm) and the BC-NC (major scattering peak centered at 77 nm) are very similar and in excellent agreement with the reported size of 77 nm for previously prepared BC-NCs. Furthermore, both the VLP-NC and BC-NC exhibit similar electrophoretic mobilities in agarose gels (Supplementary Fig. S3), whereas the free Au NPs ran faster than the NCs as expected and Transmission Electron Micrographs (TEMs) show similarity in shape and size of individual NCs (Supplementary Fig. S3C). These results indicate that VLP-NCs and BC-NCs are of equivalent size, exhibit similar bulk properties, and can be reproducibly prepared as viable scaffolds for fabrication of nanoplasmonic structures in solution.

While DLS and TEM demonstrate the similarity of the VLP-NC and BC-NC we further characterized the structures by AFM to have imaging results exactly from the clusters used for SERS measurements. The structures of the VLP-NCs and BC-NCs were characterized by AFM in air following their immobilization on EDA coated mica as shown in Fig. 2. Low resolution scans (Fig. 2A) reveal that the NCs are well dispersed on the surface without indication of significant aggregation as shown in the particle size distribution (Fig. 2B). At higher resolution clear differences between the free Au NPs and the NCs are observed. In particular, the height of the free Au NPs (*i.e.*, ~24 nm, Fig. 2C) is significantly less than that of the VLP-NCs (*i.e.*, ~45 nm, Fig. 2D) and BC-NCs (*i.e.*, ~50 nm, Fig. 2E) as expected. This greater than 2-fold increase in size of the NCs and their cross-sectional shape differences (Fig. 2F) compared to free Au NPs support the presence of Au NPs bound to the icosahedral viral capsids. Furthermore, the height profiles of the Au NP and the NCs as shown in Fig. 2F indicate minor differences between the NCs. However, the sizes of the VLP-NC and BC-NC measured by AFM on dried samples are smaller than the sizes measured by DLS (*vide supra*) of the NCs in aqueous solutions (Figs. 1B and C). These suggest some distortion of the NCs, but not total collapse of the protein capsids during immobilization and drying, consistent with recent observations noted for the VLP capsid in the absence of attached Au NPs (Jaafar et al. 2014). The similarity in shape and size of the VLP-NCs and BC-NCs further indicates that the absence of RNA in the VLP capsids does not materially affect the formation and stability of the VLP-NCs, permitting use of the simpler fabrication protocols associated with VLP-NC assembly for future work.

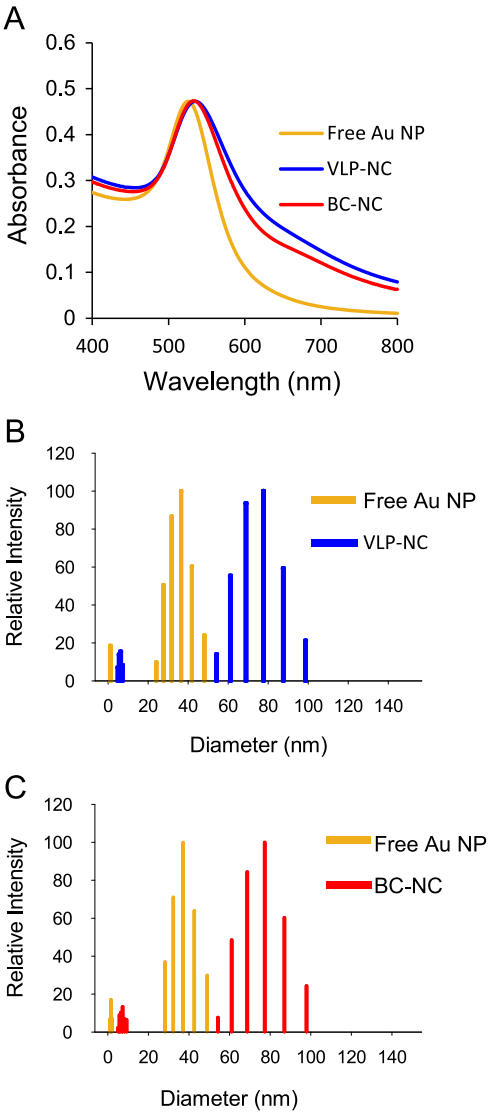

Fig. 1. Characterization of NCs in solution. (A) Visible absorption spectrum of NCs after purification vs. free Au NP treated by similar methods, data normalized relative to plasmon peak. DLS of purified: (B) VLP-NC (major peak: 78 nm) and (C) BC-NC (major peak: 77 nm). As expected the size of the NC is larger relative to the free Au NP (major peak: 37 nm) yellow histograms plotted in B and C for comparison purposes. (For interpretation of the references to color in this figure legend, the reader is referred to the web version of this article.)

For the characterization of the plasmon properties and field enhancements of the NCs, we first calculated their expected electric field distributions based on the premise that the main source of field enhancement by Au NPs involves the concentration of the electrical component of the optical field at specific locations around the NPs (Brus 2008; Henry et al. 2011). Our calculations (Section 2.7) show that the electric field around an isolated Au NP is highest at the widest part of the NP, in agreement with previous computer simulations (Jaafar et al. 2014). For example, a 3-fold field enhancement is predicted for a single 30 nm diameter Au NP (Fig. 3A), whereas a pair of 30 nm diameter Au NPs separated by 5 nm is expected to exhibit an 8-fold enhancement concentrated in the region between the NPs (*i.e.*, the hot spots located in red region of Fig. 3B and peak in Fig. 3C). Because electric field intensity is proportional to the square of field amplitude,

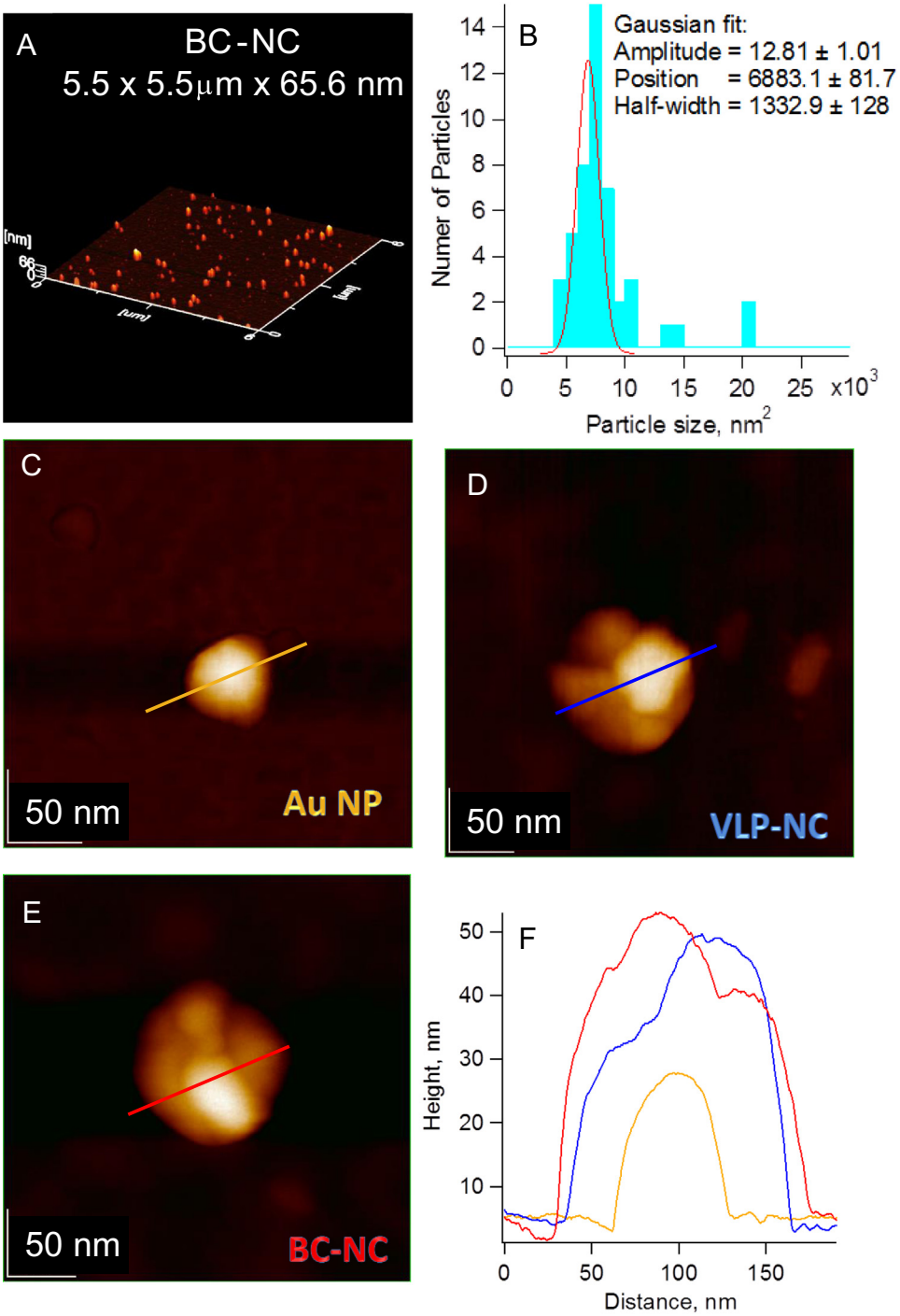

Fig. 2. AFM imaging of NCs and Au NPs on mica–silane. (A) 3D view of BC-NCs deposited on mica-silane. (B) Particle size distribution estimated by surface coverage in image and its Gaussian fit. AFM images of individual (C) Au NP, (D) VLP-NC, and (E) BC-NC (scale bars, lower left = 50 nm). Note the presence of multiple Au NPs in the VLP-NC and BC-NC images of parts D and E. (F) Height profile of individual Au NP (yellow), VLP-NC (blue), and BC-NC (red) along the lines shown in C, D, and E, respectively. (For interpretation of the references to color in this figure legend, the reader is referred to the web version of this article.)

corresponding Raman enhancements of ~9-fold and 64-fold are expected, respectively, for these structures.

Similar calculations performed for the BC-NCs (Fig. 3D–G) indicate that enhanced fields occur along lines connecting the centers of the Au NPs. Furthermore, in cases where the electric field vector is not oriented parallel to the line connecting Au NP centers of NCs, field intensity is proportional to the projection of the electric field vector onto it. Calculations of field profiles for each Au NP pair in the BC-NCs (and structurally equivalent VLP-NCs) yield *average* predicted field enhancements and energy (intensity) enhancements of ~7-fold and ~49-fold, respectively (Figs. 3F and G, Supplementary Table S1). Note that our calculations (1) apply to a NC system exposed to an oriented (polarized) optical field (electric field vector) propagating normal to the NC, and (2) include effects resulting from changes in the orientation of the electric field vector due to light scattering by the NC at fixed total energy impinging on the NC. These conditions lead to a more homogeneous field distribution, which minimizes the potential effects and contributions of local overheating at the NC surface, making the structure appealing for sensing biologicals.

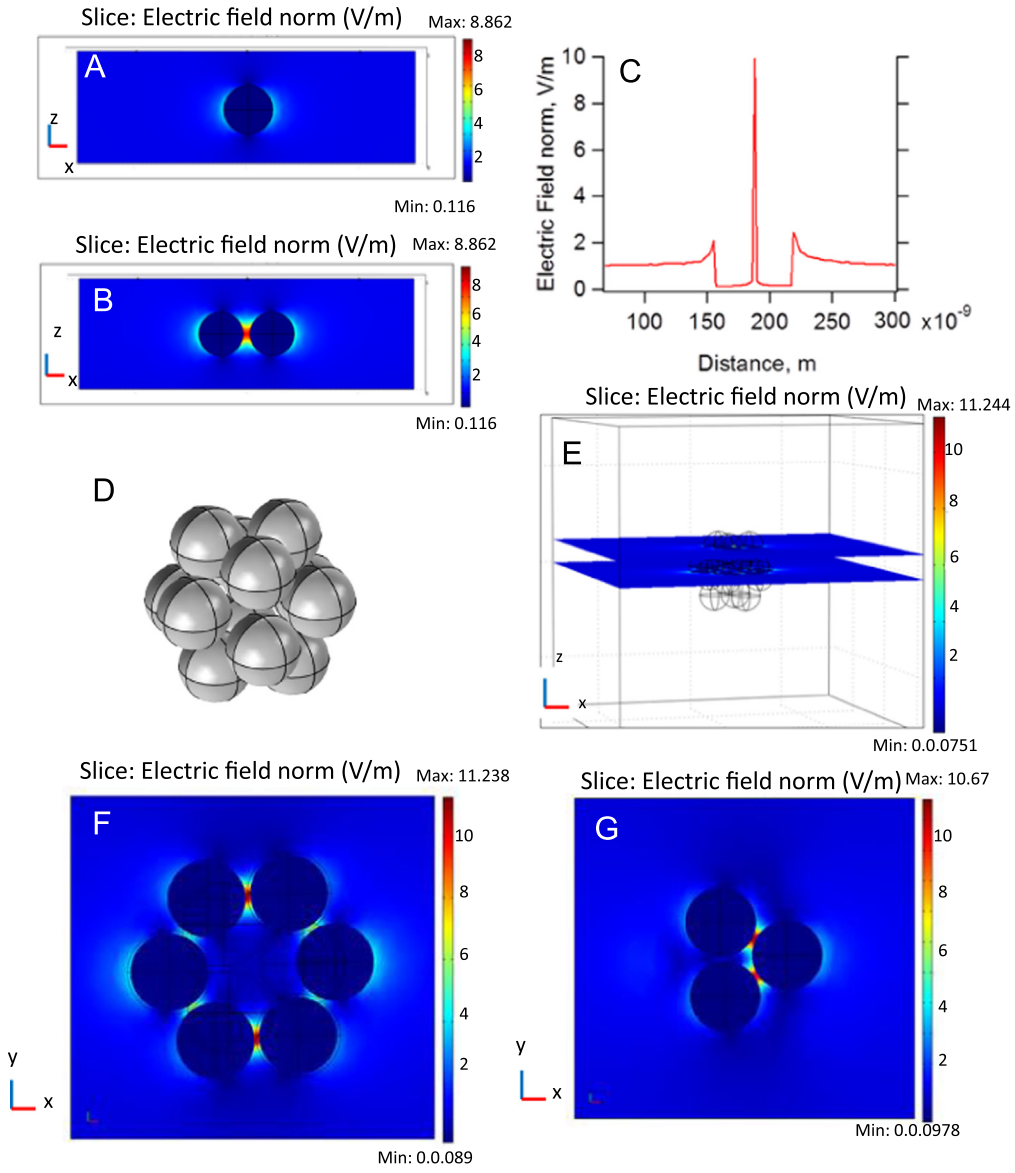

Fig. 3. Location and intensity of LSP in NCs. (A) Electric field distribution around a single Au NP with diameter 30 nm and (B) two 30 nmAu NPs separated by 5 nm. (C) Electric field profile between two spheres at the maximal field strength. (D) Artistic simulation of 12 spheres' NCs. (E) Positions of the cross-sections depicted in F and G. (F) Electric field distribution at the cross-sections corresponding to the widest part of the NC and (G) through top three Au NPs. The incident light propagates perpendicular to the plane of the cross-section and electric vector of 1 W/m is oriented along x. All calculations are done for air environment using 3D finite-element analysis.

Quantitative SERS experiments (Fig. 4) performed on individual NCs deposited onto EDA-coated mica surfaces provide an effective means to test the predictions presented in Fig. 3 and Supplementary Table S1. Although initial experiments led to *qualitatively* similar spectra for NCs deposited onto 10 nm thick planar cysteamine-Au substrates and EDA-coated mica substrates, we selected EDA-coated mica substrates for use (1) to avoid any possible interference from the Au substrate plasmon, (2) to have an atomically flat substrate surface, and (3) to take advantage of naturally occurring mica Raman peaks as internal standards for quantitative analysis of our NC systems' behaviors. Samples were prepared by treating EDA-coated mica substrates with aqueous dispersions containing different VLP-NC (or BC-NC) concentrations (Section 2.5) to control NC–NC separations, which were probed by optical microscopy *via* light scattering from individual NCs. We found that, for our systems, use of diluted samples and analysis with a 100 × objective (Lebedev et al. 2014a, b) provides optimal spatial resolution, as well as laser focusing and efficient light collection from individual NCs during subsequent SERS measurements. It is important to note that we used AFM (Fig. 2) to characterize the samples just prior to SERS experiments, ensuring sample quality at exactly the same conditions and surfaces used for SERS detection. AFM topographic scans of samples used for SERS measurements indicated the presence of 3–7 NCs in a $2 \times 2\ \mu m^2$ substrate area, corresponding to NC–NC separations $> 1\ \mu m$ adequate for observation of single NC SERS signals using our instrument.

Fig. 4A illustrates representative average Raman spectra (each spectrum was recorded three (3) times and averaged; standard deviation for intensity values was 20%, 785 nm excitation) of the VLP-NC (blue spectrum, corresponding peaks in black text), BC-NC (red spectrum), and lone Au NPs (yellow spectrum, corresponding peaks in yellow text), as well as the underlying mica substrate (green spectrum). Major peaks observed for the VLP-NC (empty capsids, Figs. 4A and B) at 432, 555, 898, 967, 1004, 1077, 1145, 1270, 1353, 1380, 1420, 1455, and 1498 cm^{-1} are absent in the spectrum of the isolated Au NPs (Figs. 4A and C), indicating that these peaks are associated with the capsid protein. These peaks

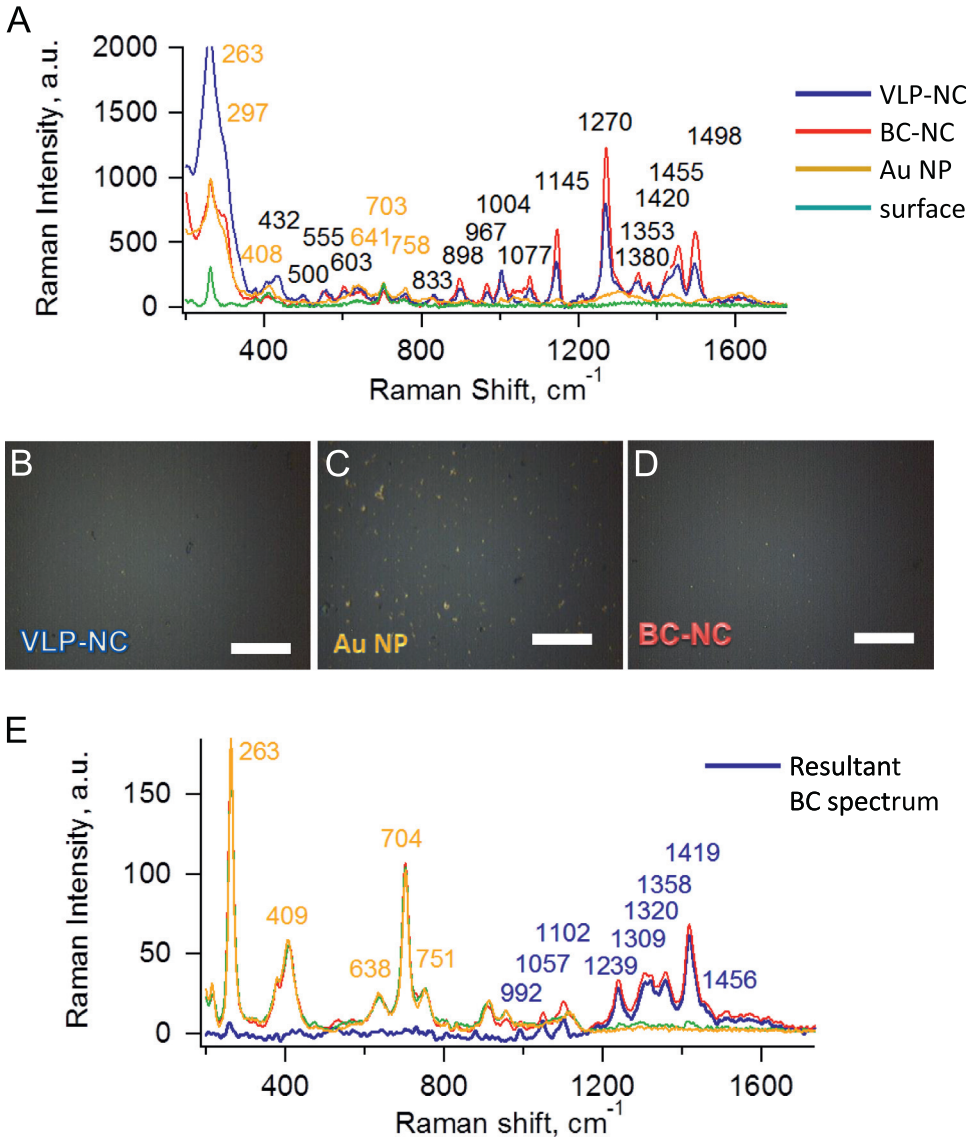

Fig. 4. Average Raman spectra of individual NCs, Au NPs, and BC on mica-silane. (A) Raman spectra of VLP-NC (blue), Au NPs (yellow) and BC-NC (red) on mica-silane surfaces. The spectra are collected from the individual bright spots (isolated nanoclusters) shown in panels B, C, and D, respectively. The spectrum of bare mica is shown in green. Optical images: (B) VLP-NC, (C) Au NPs, and (D) BC-NC on mica-silane showing bright spots of light scattering from Au NPs; scale bar 10 μm. (E) Raman spectra of BC without Au NPs (negative control) on mica-silane (red), the same sample in an area lacking BC (yellow), and bare mica-silane (green). The blue line represents "pure" non-enhanced BC spectrum generated by subtraction of mica-silane from the total BC-mica-silane spectrum. Note the about *ten-fold* difference in Raman intensity scale (y axis) between the BC-NC in panel A (red) and the BC lacking Au NPs in panel E (blue). Average spectra resulted from 3 measurements. (For interpretation of the references to color in this figure legend, the reader is referred to the web version of this article.)

are highly reproducible and identical to those observed for the BC-NC (RNA-filled capsids, Figs. 4A and D). The lack of additional peaks corresponding to efficient Raman enhancement of the RNA in the BC-NC spectrum further supports our calculations indicating that the electromagnetic field required for Raman enhancement is localized between the Au NPs (*i.e.*, the hot spots) on the capsid surface. Therefore only the protein peaks are enhanced. The remaining peaks observed at 263, 410, 651, 703, and 760 cm^{-1} in the VLP-NC spectrum are identical to those observed for mica (green spectrum, Fig. 4A), while the peak at 297 cm^{-1} appears to be associated with Au NP (yellow spectrum, Fig. 4A).

Figs. 4A and E permit comparison of the Raman spectra on the mica surface of the BC-NC to that of the bare BC virus capsids, providing an estimate for the efficiency of the light field concentration in our NCs. Subtraction of the spectrum associated with the mica substrate (green spectrum) from that of the BC capsid on mica (red spectrum) in Fig. 4E provides an estimate for the spectrum of non-enhanced BC capsids (blue spectrum and corresponding blue peaks denoted in blue text, Fig. 4E). Comparison of this BC capsid non-enhanced Raman spectrum (blue spectrum, Fig. 4E) to that for the BC-NC spectrum (red spectrum, Fig. 4A) indicates that the *average* intensity of the capsid peaks is at least *10-fold less* without Au NPs, suggesting a *SERS enhancement in the BC-NC of at least 10-fold*. It is important to emphasize that the broad peak around ~263 cm^{-1} present in the VLP-NC, BC-NC, and Au NP spectra (blue, red, and yellow Fig. 4A) is not as sharp as the plain mica peak at 263 cm^{-1}. Therefore, the ~263 cm^{-1} broad peak in these gold containing samples has potentially a contribution from another component in the system that we anticipate to be thioctic acid (a.k.a. lipoic acid) (Busby et al. 1999) used during the sample preparation. For this reason, we did not use the peak at 263 cm^{-1} for SERS enhancement calculations of the protein peaks.

A critical issue for the successful use of our NCs as SERS tracers

or biosensors is their ability to detect species with wide-ranging structural complexity present in their external environment. The presence of Raman signals from the protein capsids noted in Fig. 4 suggests that capsid protein occupies a portion of the hot spot regions between adjacent Au NPs inside the NCs. In addition, on the exterior of the NCs steric effects associated with the size and spacing of the Au NPs in the NCs, as well as electrostatic effects due to the presence of ionized thioctic acid species stabilizing the NC dispersions, may affect access to the hot spots. Therefore, the questions naturally arise as to whether external analytes can enter the hot spot regions on our NCs for efficient SERS enhancement and detection and if those analytes on the exterior of the NC would affect the protein signals associated with protein capsid inside the plasmonic NC.

In order to address these questions, we examined the ability of our mica-immobilized BC-NCs to detect M13mp18 single-stranded DNA (ssDNA circular, New England Biolabs, MA) as a commercially available test species delivered from aqueous solution (pH ~6.8). In general, M13mp18 ssDNA provides an attractive test analyte for several reasons. For example, Raman signatures of the nucleic acids comprising DNA are well characterized both experimentally (Dijanošić et al. 2014; Hobro et al. 2013; Kuzmin et al. 2013; Miljanić et al. 2015) and theoretically (Arivazhagan et al. 2014). Specifically, the DNA Raman spectrum exhibits both ribose (~900 cm^{-1}) and several high frequency nucleotide modes located in regions free from strong vibrational components associated with the VLP-NC, BC-NC, and mica Raman modes (*e.g.*, 1500–1600 cm^{-1}), facilitating rapid identification of DNA-related bands during the SERS studies. As a circular ssDNA comprising 7249 nucleotide bases, M13mp18 ssDNA additionally provides a target of expected high steric hindrance in comparison to small molecules. As previously reported, the height of the M13mp18 ssDNA corresponds to 0.2–0.3 nm (Tanaka and Kawai 2009) and a contour length of 2200 nm, consistent with the linearized molecule (Woolley et al. 2000). Since we are exploring the possibility to extract structural information we kept M13mp18 ssDNA in its intact circular form, which is known to form 3D structures (Ayora et al. 2002). Furthermore, electrostatic repulsion between its anionic phosphate backbone and thioctic acid carboxylate groups present on the Au NPs in the NCs may influence M13mp18 ssDNA access to the hot spot regions between adjacent Au NPs present on the NCs. Consequently, M13mp18 ssDNA provides a rigorous, challenging analyte to test our NC systems for biosensing.

Fig. 5A summarizes the average SERS results (each spectrum was recorded three (3) times and averaged) for our test M13mp18 ssDNA analyte (785 nm excitation), with Fig. 5B highlighting the 1400–1600 cm^{-1} region where DNA nucleic acid Raman signals are dominant and corresponding BC capsid signals are relatively muted. Spectra shown have been obtained from dried BC-NC containing samples that were exposed to 1 μl aqueous aliquots of 0.25–250 ng μl^{-1} M13mp18 ssDNA (4 × 4 arrays), with usable Raman signals observed for all samples. A Raman spectrum that exhibits signals due solely to the mica substrate, with no discernible peaks attributable to the M13mp18 ssDNA in the 1400–1600 cm^{-1} region, is observed for M13mp18 ssDNA (Figs. 5A and B, violet spectrum) deposited directly onto the mica substrate (1 μl, 250 ng μl^{-1}, Fig. 5C), consistent with the lack of M13mp18 ssDNA signal enhancement expected in the absence of BC-NCs.

In contrast, the Raman spectrum of the BC-NC on the mica substrate (Figs. 5A and B, red spectra, and Fig. 5D), is clearly observed (*cf*, Figs. 4A and E) in the absence of added M13mp18 ssDNA, as expected. Subsequent addition of M13mp18 ssDNA (1 μl of 0.25 ng μl^{-1}) to the BC-NC substrate (Fig. 5E) leads to substantial changes in the BC-NC Raman spectrum, as shown by the light and dark blue spectra (Figs. 5A and B) each taken at two *separate* BC-NC sites on the surface. In particular, new Raman

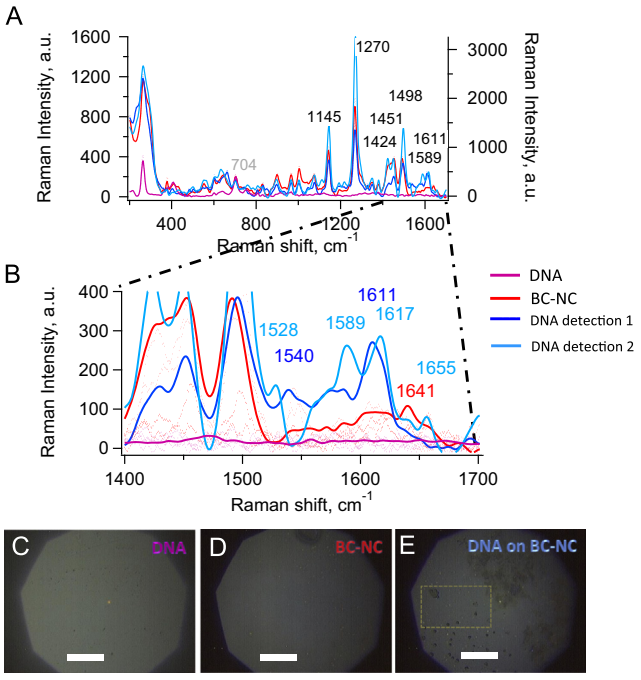

Fig. 5. Detection of DNA by individual BC-NCs. (A) Averaged Raman spectra of plain DNA (violet), BC-NC (red), and BC-NC after addition of DNA (light and dark blue; DNA detection 1 and 2 are done individually in separate clusters) on mica-silane surfaces collected from individual NCs corresponding to samples shown in panels C, D, and E (dark blue), respectively. The spectra are normalized for mica Raman peak 703 cm^{-1}. (B) Expanded area (1400–1700 cm^{-1}) with specific DNA Raman peaks. The single BC-NC enhanced DNA-specific Raman peaks appear at 1589, and 1611 cm^{-1}. Optical images of mica-silane surfaces with (C) DNA, (D) BC-NC, and (E) BC-NC+DNA (for DNA detection). The yellow spot in the middle of C is the excitation light beam used in experiments, while bright spots in D and E are due to the background white light scattered from BC-NC gold nanoparticles. Scale bar 10 μm. Average spectra resulted from 3 measurements. Gray square in panel E (bottom left) encloses a typical area for the assays. Any area showing defects from the surface was avoided for SERS analysis. (For interpretation of the references to color in this figure legend, the reader is referred to the web version of this article.)

bands at 1589 and 1611 cm^{-1} appear in the 1500–1600 cm^{-1} region free from strong BC capsids protein bands, consistent with the presence of DNA. However, the intensities of these DNA-specific peaks vary when testing (*e.g.*, 1589 cm^{-1} peak in light blue *vs.* dark blue spectrum, Fig. 5B) for spectra taken from two different BC-NC+DNA individual particles. In addition, the intensities of the Raman spectra at certain existing BC capsid protein bands (*e.g.*, Fig. 5A, 1145, 1270, and 1498 cm^{-1} peaks where overlapping DNA peaks are located) are also similarly modulated in the presence of the M13mp18 ssDNA sample. Such SERS spectrum variations are expected due to potentially different DNA and/or protein capsid orientation and/or displacement effects during DNA entry into the hot spot regions on different NCs. The fact that we detect M13mp18 ssDNA only *via* its corresponding SERS signals in Fig. 5 provides proof-of-principle for use of our NCs as SERS platforms for detection of sterically and electrostatically challenging biological analytes.

4. Conclusions

In the current work, we have demonstrated that VLP-NC and BC-NC are robust bio-photonic complexes that can be used for local electromagnetic field concentration and spatially-resolved Raman enhancement for detection and identification of both the virus capsid protein and surrounding molecules, like DNA. In the latter case the enhancement is more than an order of magnitude and is substantially superior to the enhancement observed with an

individual Au NP allowing us to readily detect down to 0.25 ng/μl of M13mp18 ssDNA. The NCs have a strong, clear, reproducible, and stable Raman signature which comes from the internal protein shell that is retained as an internal standard even in the presence of external analytes bound to the "hot spots". Based on our proof-of-principle, the NCs are good biosensor candidates for *in vitro* and/or *in vivo* studies where the low toxicity of Au NPs and the small sizes of the NCs are of great advantage. Future directions of this research may comprise the incorporation of specific receptors, antibodies, or antimicrobial peptides into the nanoclusters to increase its selectivity in complex mixtures.

Acknowledgements

CMS thanks V. Reddy and A.S. Blum for scientific discussions and J. Fontana for TEM images. CMS acknowledges financial support from the US Office of Naval Research. This work was also supported by grants BB/I002294/1 and BB/J004561/1 from the UK Biotechnology and Biological Sciences Research Council (BBSRC) and the John Innes Foundation (YM and GPL).

Appendix A. Supplementary material

Supplementary data associated with this article can be found in the online version at http://dx.doi.org/10.1016/j.bios.2015.09.032.

References

Aćimović, S.S., Kreuzer, M.P., González, M.U., Quidant, R., 2009. ACS Nano 3 (5), 1231–1237.
Aljabali, A.A.A., Sainsbury, F., Lomonossoff, G.P., Evans, D.J., 2010. Small 6 (7), 818–821.
Alù, A., Engheta, N., 2009. Opt. Express 17 (7), 5723–5730.
Arivazhagan, M., Kavitha, R., Subhasini, V.P., 2014. Spectrochim. Acta Part A 130, 502–515.
Ayora, S., Missich, R., Mesa, P., Lurz, R., Yang, S., Egelman, E.H., Alonso, J.C., 2002 277 (39), 35969–35979.
Bahns, J.T., Guo, Q., Montgomery, J.M., Gray, S.K., Jaeger, H.M., Chen, L., 2009. J. Phys. Chem. C 113 (26), 11190–11197.
Barrow, S.J., Wei, X., Baldauf, J.S., Funston, A.M., Mulvaney, P., 2012. Nat. Commun., 3, Article No. 1275, 10.1038/ncomms2289.
Becker, M., Stelzner, T., Steinbrück, A., Berger, A., Liu, J., Lerose, D., Gösele, U., Christiansen, S., 2009. ChemPhysChem 10 (8), 1219–1224.
Blum, A.S., Soto, C.M., Sapsford, K.E., Wilson, C.D., Moore, M.H., Ratna, B.R., 2011. Biosens. Bioelectron. 26 (6), 2852–2857.
Blum, A.S., Soto, C.M., Wilson, C.D., Amsinck, C., Franzon, P., Ratna, B.R., 2007. IEEE Trans. Nanobiosci. 6 (4), 270–274.
Blum, A.S., Soto, C.M., Wilson, C.D., Brower, T.L., Pollack, S.K., Schull, T.L., Chatterji, A., Lin, T.W., Johnson, J.E., Amsinck, C., Franzon, P., Shashidhar, R., Ratna, B.R., 2005 1(7), 702–706.
Blum, A.S., Soto, C.M., Wilson, C.D., Cole, J.D., Kim, M., Gnade, B., Chatterji, A., Ochoa, W.F., Lin, T.W., Johnson, J.E., Ratna, B.R., 2004 4(5), 867–870.
Blum, A.S., Soto, C.M., Wilson, C.D., Whitley, J.L., Moore, M.H., Sapsford, K.E., Lin, T. W., Chatterji, A., Johnson, J.E., Ratna, B.R., 2006. Nanotechnology 17 (20), 5073–5079.
Brus, L., 2008. Acc. Chem. Res. 41 (12), 1742–1749.
Busby, R.W., Schelvis, J.P.M., Yu, D.S., Babcock, G.T., Marletta, M.A., 1999 121, 4706–4707.
Busson, M.P., Rolly, B., Stout, B., Bonod, N., Larquet, E., Polman, A., Bidault, S., 2011. Nano Lett. 11 (11), 5060–5065.
Chatterji, A., Ochoa, W.F., Paine, M., Ratna, B.R., Johnson, J.E., Lin, T.W., 2004. Chem. Biol. 11 (6), 855–863.
Chen, F., Spano, A., Goodman, B.E., Blasier, K.R., Sabat, A., Jeffery, E., Norris, A., Shabanowitz, J., Hunt, D.F., Lebedev, N., 2009. J. Proteome Res. 8 (2), 967–973.
De Angelis, F., Gentile, F., Mecarini, F., Das, G., Moretti, M., Candeloro, P., Coluccio, M. L., Cojoc, G., Accardo, A., Liberale, C., Zaccaria, R.P., Perozziello, G., Tirinato, L., Toma, A., Cuda, G., Cingolani, R., Di Fabrizio, E., 2011. Nat. Photon 5 (11), 682–687.
Dijanošić, A., Miljanić, S., Piantanida, I., González-García, J., García-España, E., 2014. J. Raman Spectrosc. 45 (10), 863–872.
Dressick, W.J., Kondracki, L.M., Chen, M.-S., Brandow, S.L., Matijević, E., Calvert, J.M., 1996. Colloids Surf. A 108 (1), 101–111.
Driskell, J.D., Shanmukh, S., Liu, Y., Chaney, S.B., Tang, X.-J., Zhao, Y.-P., Dluhy, R.A., 2008. J. Phys. Chem. C 112 (4), 895–901.
Engheta, N., 2007. Science 317, 1698–1702.
Fan, J.A., Wu, C., Bao, K., Bao, J., Bardhan, R., Halas, N.J., Manoharan, V.N., Nordlander, P., Shvets, G., Capasso, F., 2010. Science 328, 1135–1138.
Ferrando, R., Jellinek, J., Johnston, R.L., 2008. Chem. Rev. 108 (3), 845–910.
Fleischmann, M., Hendra, P.J., McQuillan, A.J., 1974. Chem. Phys. Lett. 26 (2), 163–166.
Fontana, J., Dressick, W.J., Phelps, J., Johnson, J.E., Rendell, R.W., Sampson, T., Ratna, B.R., Soto, C.M., 2014. Small 10 (15), 3058–3063.
Henry, A.-I., Bingham, J.M., Ringe, E., Marks, L.D., Schatz, G.C., Van Duyne, R.P., 2011. J. Phys. Chem. C 115 (19), 9291–9305.
Hobro, A.J., Standley, D.M., Ahmad, S., Smith, N.I., 2013. Phys. Chem. Chem. Phys. 15 (31), 13199–13208.
Jaafar, M., Aljabali, A.A.A., Berlanga, I., Mas-Balleste, R., Saxena, P., Warren, S., Lomonossoff, G.P., Evans, D.J., de Pablo, P.J., 2014. ACS Appl. Mater. Interfaces 6, 20936–20942.
Jin, J., 2002. The Finite Element Method in Electromagnetics. John Wiley & Sons Inc., Hoboken, New Jersey, USA.
Kuzmin, A.N., Pliss, A., Kachynski, A.V., 2013. J. Raman Spectrosc. 44 (2), 198–204.
Lebedev, N., Strycharz-Glaven, S.M., Tender, L.M., 2014a. Front. Energy Res. 2, 34.
Lebedev, N., Strycharz-Glaven, S.M., Tender, L.M., 2014b. ChemPhysChem 15 (2), 320–327.
Lin, T., Chen, Z., Usha, R., Stauffacher, C.V., Dai, J., Schmidt, T., Johnson, J.E., 1999. Virology 265, 20–35.
Malvadkar, N.A., Demirel, G., Poss, M., Javed, A., Dressick, W.J., Demirel, M.C., 2010. J. Phys. Chem. C 114 (24), 10730–10738.
Miljanić, S., Dijanošić, A., Matić, I., 2015. Spectrochim. Acta Part A 137, 1357–1362.
Mu, C., Zhang, J.-P., Xu, D., 2010. Nanotechnology 21 (1), Article No. 015604.
Ortiz, N., Skrabalak, S.E., 2014. Langmuir 30 (23), 6649–6659.
Palik, D.E., 1998. Handbook of optical constants of solids. Academic Press, San Diego.
Sainsbury, F., Saxena, P., Aljabali, A.A.A., Saunders, K., Evans, D.J., Lomonossoff, G.P., 2014. Genetic Engineering and Characterization of Cowpea Mosaic Virus Empty Virus-Like Particles. In: Lin, B., Ratna, B. (Eds.), Virus Hybrids as Nanomaterials Methods Mol. Biol.. Humana Press, pp. 139–153.
Sarkar, S., Dutta, S., Pal, T., 2014. J. Phys. Chem. C 118 (48), 28152–28161.
Schlücker, S., 2014. Angew. Chem. Int. Ed. Engl. 53 (19), 4756–4795.
Shao, Q., Que, R., Shao, M., Cheng, L., Lee, S.-T., 2012. Adv. Funct. Mater. 22 (10), 2067–2070.
Smith, M.T., Hawes, A.K., Bundy, B.C., 2013. Curr. Opin. Biotechnol. 24, 620–626.
Soto, C.M., 2014. A programmable Fluorescence Viral Nanoblock: Sensing Made Easy in a Single Step. In: Lin, B., Ratna, B.R. (Eds.), Virus hybrids as nanomaterials Methods and Protocols. Humana Press Springer publishing group, New York, USA, pp. 155–172.
Soto, C.M., Ratna, B.R., 2010. Curr. Opin. Biotechnol. 21 (4), 426–438.
Spano, A.J., Chen, F.S., Goodman, B.E., Sabat, A.E., Simon, M.N., Wall, J.S., Correia, J.J., McIvor, W., Newcomb, W.W., Brown, J.C., Schnur, J.M., Lebedev, N., 2007. Virology 364, 95–102.
Steinmetz, N.F., Evans, D.J., Lomonossoff, G.P., 2007. Chembiochem 8 (10), 1131–1136.
Tan, J.M.R., Ruan, J.J., Lee, H.K., Phang, I.Y., Ling, X.Y., 2014. Phys. Chem. Chem. Phys. 16 (48), 26983–26990.
Tanaka, H., Kawai, T., 2009 4, 518–522.
Urban, A.S., Shen, X., Wang, Y., Large, N., Wang, H., Knight, M.W., Nordlander, P., Chen, H., Halas, N.J., 2013. Nano Lett. 13, 4399–4403.
Wang, Y., Yan, B., Chen, L., 2013. Chem. Rev. 113 (3), 1391–1428.
Woolley, A.T., Guillemette, C., Cheung, C.L., Housman, D.E., Lieber, C.M., 2000 18, 760–763.
Yang, Q., Deng, M., Li, H., Li, M., Zhang, C., Shen, W., Li, Y., Guo, D., Song, Y., 2015. Nanoscale 7 (2), 421–425.
Zahr, O.K., Blum, A.S., 2012. Nano Lett. 12 (2), 629–633.
Zhao, P., Li, N., Astruc, D., 2013a. Coord. Chem. Rev. 257 (3–4), 638–665.
Zhao, Y., Xu, L., Liz-Marzán, L.M., Kuang, H., Ma, W., Asenjo-García, A., García de Abajo, F.J., Kotov, N.A., Wang, L., Xu, C., 2013b. J. Phys. Chem. Lett. 4 (4), 641–647.
Zhou, J.C., Soto, C.M., Chen, M.S., Bruckman, M.A., Moore, M.H., Barry, E., Ratna, B.R., Pehrsson, P.E., Spies, B.R., Confer, T.S., 2012. J. Nanobiotechnol., 10, Article No. 18.